Economic Geology
Vol. 89, 1994, pp. 361–380

Time-Pressure and Temperature Constraints on the Formation of Colombian Emeralds: An $^{40}Ar/^{39}Ar$ Laser Microprobe and Fluid Inclusion Study*

A. CHEILLETZ,

Centre de Recherches Pétrographiques et Géochimiques, UPR A 6821, et Ecole Nationale Supérieure de Géologie, 15 rue Notre Dame des Pauvres, B.P. 20, 54501 Vandoeuvre-lès-Nancy Cedex, France

G. FÉRAUD,

Institut de Géodynamique, URA CNRS 1279, Université de Nice, Parc Valrose, 06034 Nice Cedex, France

G. GIULIANI,

Centre de Recherches Pétrographiques et Géochimiques, UPR A 6821, 15 rue Notre Dame des Pauvres, B.P. 20, 54501 Vandoeuvre-lès-Nancy Cedex, France, and ORSTOM, Département TOA, UR 1H, 213 rue La Fayette, 75480 Paris Cedex, France

AND C. T. RODRIGUEZ**

MINERALCO S.A., calle 32 n° 1307, Bogotá, Colombia

Abstract

Two Colombian deposits belonging to the western emerald belt of the Eastern Cordillera, namely Coscuez and Quipama-Muzo, hosted in Lower Cretaceous black shales, have been dated for the first time by $^{40}Ar/^{39}Ar$ induction and laser microprobe methods on contemporaneous greenish Cr-V-rich K mica aggregates consisting of muscovite as a dominant phase ± kaolinite, ± paragonite, ± quartz, ± albite, and ± chlorite, pyrite, and calcite. Contamination of the K mica aggregates by wall-rock impurities is eliminated by in situ $^{40}Ar/^{39}Ar$ laser spot analysis. Two distinct plateau and spot fusion ages of 35 to 38 Ma and 31.5 to 32.6 Ma were obtained for the Coscuez and Quipama samples, respectively, i.e., a late Eocene to early Oligocene age. Concordant conventional K-Ar ages show that in spite of the small size of these micas, they did not suffer significant ^{39}Ar loss due to recoil during irradiation of the samples. Internal ^{39}Ar recoil may explain the slight disturbances observed on the age spectra. Microthermometry, Raman spectroscopy, and SEM experiments performed on fluid inclusions trapped in emerald crystals from the Coscuez deposit show that the hydrothermal fluids are complex H_2O-NaCl-$CaCl_2$-KCl-CO_2-N_2 brines (38 wt % NaCl equiv). Constrained by the $^{40}Ar/^{39}Ar$ age determinations, the Eastern Cordillera subsiding model, and the assumption of lithostatic confining pressures, isochoric extrapolations lead to a pressure-temperature estimate of 1.06 to 1.12 kbars and 290° to 360°C for the emerald deposition. The P-T evaluation is in agreement with the paragenesis accompanying the emerald deposition.

A moderate-temperature epigenetic hydrothermal-sedimentary model is proposed for Colombian emerald genesis. This model makes use of the following points: (1) the depth of hydrothermal circulation within the Lower Cretaceous series, (2) a basinal origin of mineralizing fluids as inferred from oxygen and carbon isotope data, (3) an evaporitic source for the NaCl sulfate-rich brines trapped within emerald crystals, as deduced from sulfur isotope data, (4) a likely source of the metallic components, and particularly Be, Cr, and V, being the black shale reservoir, and (5) the timing of hydrothermal circulation and emerald vein formation in relation to Eastern Cordillera tectonic evolution——in particular, the strong shortening episode beginning during the Eocene.

Introduction

THE emerald deposits of Colombia are located 50 to 80 km northeast of Bogotá in the Andean mountain system (Fig. 1) within two mineralized belts (Forero, 1987): an eastern belt encompassing the districts of Gachalá and Chivor, and a western belt containing the Coscuez, Quipama, and La Palma districts. During the late 1990s, Colombia ranked first in the world in emerald production, yielding approximately 10 millions carats or two tons. The unique characteristic of the Colombian emerald deposits consists in their geologic setting: they are enclosed within the Lower Cretaceous weakly metamorphosed black shales of the Eastern Cordillera chain. This causes a marked

* CRPG contribution 940.

** Present address: Promining LTDA, Carrera 15 no. 95–64, Of. 410, Bogotá, Colombia.

0361-0128/94/1554/361-20$4.00

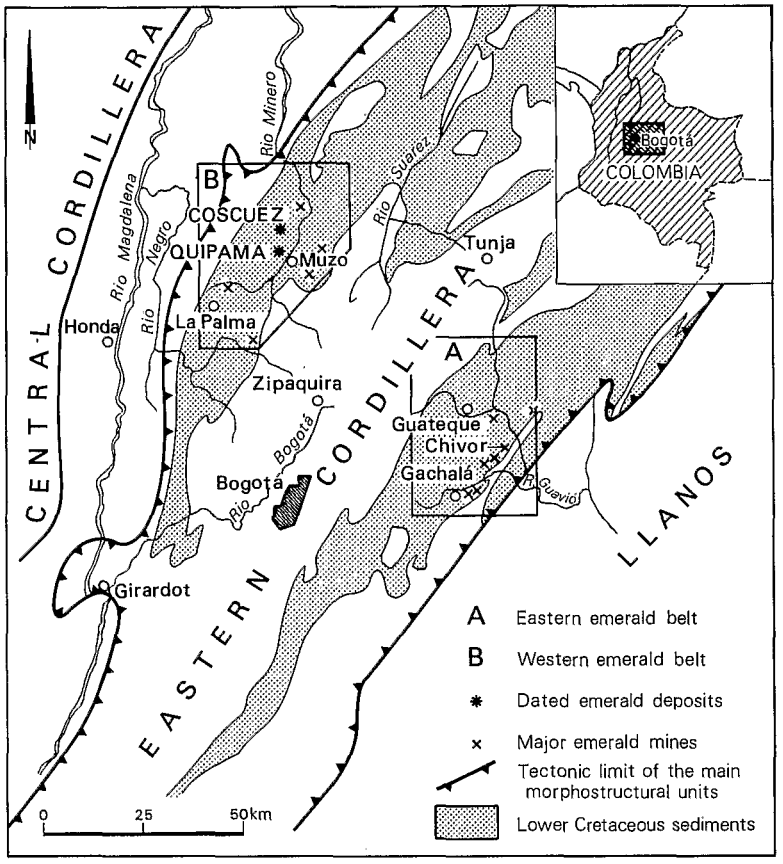

FIG. 1. Geology the two emerald belts of Colombia (adapted from Colleta et al., 1990).

contrast with most other emerald deposits in the world that are predominantly hosted by suture zones or greenstone terranes mostly in highly metamorphosed cratonic areas (Kazmi and Snee, 1989). Moreover, in these geotectonic environments, the sources of beryllium and chromium-vanadium necessary to produce that variety of green-blue beryl are likely found in pegmatites and ultramafic volcanic rocks, respectively, when they are juxtaposed and interact during tectonic phases. This has been clearly demonstrated for the Brazilian deposits for instance (Rudowski et al., 1987; Giuliani et al., 1990a). However, neither pegmatite nor ultramafic volcanic rocks have been found in the vicinity of the Colombian deposits.

A wide concensus appears today for a hydrothermal model in the genesis of the Colombian deposits (Gubelin, 1957; Touray and Poirot, 1968; Rosasco and Roedder, 1979; Ottaway and Wicks, 1986; Kozlowski et al., 1988, 1991a, b). A preliminary microthermometry, Raman spectroscopy, and SEM study of fluid inclusions from the La Vega-San Juan and Coscuez deposits (Giuliani et al., 1990c, 1992, 1993) revealed the presence of chemically homogeneous hypersaline complex brines (NaCl-KCl-$CaCl_2$, up to 40 wt % NaCl equiv) associated with emerald deposition. However, controversies still exist concerning the temperature-pressure conditions of formation deduced from fluid inclusion data; Kozlowski et al. (1988) and Roedder (1982, 1984) proposed temperatures higher than 500°C, implying a hypothetical genetic relationship of mineralizing brines with a deep-seated pegmatitic source. In fact, it appears that an independent estimate of pressure is necessary to determine adequately the pressure correction and thus interprete the fluid inclusion data. The age of mineralization also appears to be a crucial parameter in assessing the thickness of overburden prevailing in the Eastern Cordillera basin at the time of emerald deposition, and thus for providing a correlative pressure estimate. One hypothesis attributes an Early Cretaceous age to the emerald mineralization, which could be related to the synchronous emplacement of basic magmas in the Eastern Cordillera dated at 115 to 118 Ma by conventional K-Ar on amphiboles (Fabre and Delaloye, 1983). In the Eastern Cordillera, the Early Cretaceous is characterized by a strong rifting period and basin formation (Fabre, 1987) accompanied by normal faulting, high thermal

anomalies, and basin connate water drainage: such processes could have contributed to the formation of emerald deposits as well. A second hypothesis, based on relative dating by field crosscutting relationships, relates emerald mineralization to the Tertiary major tectonic and faulting period, correlated with the emplacement of postulated post-Eocene rhyolitic intrusions (Escovar, 1979).

This paper presents the first ages of Colombian emerald-bearing veins in two deposits of the western belt, namely Coscuez and Quipama, based on a $^{40}Ar/^{39}Ar$ laser microprobe investigation; and an estimate of the pressures and temperatures associated with emerald mineralization, based on microthermometric data from fluid inclusions at the Coscuez deposit.

Geologic Setting

The Eastern Cordillera of Colombia constitutes a slightly folded chain (Campbell and Bürgl, 1965; Julivert, 1970) overthrusting to the east the Llanos basin and to the west the Central Magdalena basin (Fig. 1). The major part of the Eastern Cordillera is represented by thick Cretaceous to lower Tertiary series accumulated into highly subsiding basins in response to lithospheric thinning and related crustal extension (Fabre, 1987). These basins have been deformed and uplifted during Tertiary Andean tectonic episodes.

The two main emerald-producing zones of the western belt, Coscuez and Quipama-Muzo (Fig. 1), have been selected for our study. The regional geology of the western area is much less well known than that of the eastern belt (Ulloa and Rodriguez, 1979), but the stratigraphic sequence of the Cretaceous formations presented in this paper is elaborated following the geologic synthesis of emerald deposits by Forero (1987).

The Coscuez mine

Emerald mineralization occurs in the Hauterivian-Barremian Pajá formation (Fig. 2). In the mining area, the series is composed of carbonaceous shales overlain by siliceous shales. The mineralization is hosted by a complex fracture system represented by veins, banded stratiform lenses, and breccias. The mineralized veins constitute two sets of fractures oriented at N 10° E and N 140° E crosscut by later faulting at N 20° E (the La Negra and Desaguadero faults). Hydrofracturing is recognized as a major process of breccia development (Giuliani et al., 1990b). The hydrothermal fluid circulation is accompanied by intense fluid-rock interaction and metasomatic alteration of the enclosing black shales (Baker, 1975; Beus, 1979; Giuliani et al., 1990b) consisting of carbonatization, albitization, and pyritization halos developed around the emerald-bearing carbonate vein network.

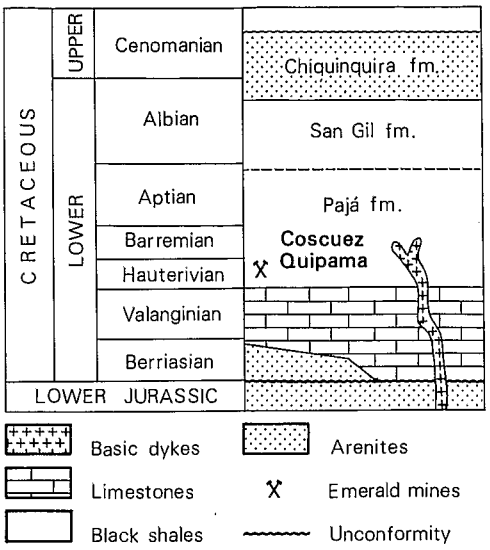

FIG. 2. Lithostratigraphic chart of the Cretaceous units of the eastern emerald belt of Colombia (modified from Forero, 1987).

The Quipama mines

The Quipama mines are composed of numerous working areas situated on both sides of the Rio Minero in the vicinity of the village of Muzo (Oppenheim, 1948). The major ones are Cincho, Palo Blanco, Massato, Aguardiente, Puerto Arturo, Tequendama, El Indio, and Las Pavas. Sample G 65 used for the present study comes from the Cincho Bajo area which belongs to the Coexmina property. The stratigraphic sequence and hydrothermal metasomatic phenomena are the same as in the Coscuez district. The Cincho field is situated between the two major Aguardiente and Animas northeast-southwest-trending faults on the right bank of the Rio Minero. The productive zone is characterized by three sets of fractures at N 0°–10° E, N 40°–70° E, and N 110°–130° E filled by calcite, dolomite, REE dolomite, pyrite, quartz, albite, and greenish K mica.

$^{40}Ar/^{39}Ar$ Laser Microprobe Dating

Sample description

Paragenetic relationships: The more extensive emerald-bearing structure is represented by a stockwork of 2- to 5-cm-wide extension fractures in the black shales. These veins show a typical mineral-banded filling constituted by calcite, pyrite, albite, dolomite, REE dolomite (parisite), fluorite, quartz, barite, and a greenish to white K mica sometimes incorrectly described as pyrophyllite. The K mica is deposited as 2- to 3-mm-wide patches on both walls of the veins followed toward the center by fibrous or euhedral calcite precipitation (Fig. 3). Calcite is the most abundant gangue mineral, its fibrous habit rep-

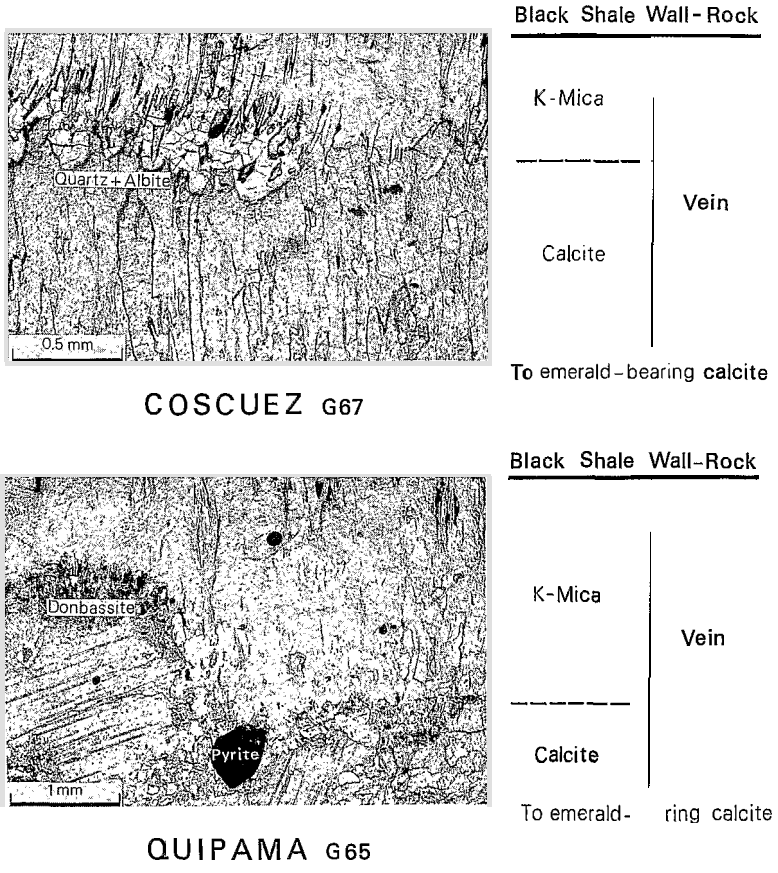

FIG. 3. Thin section of the contact between the black shale wall-rock and the emerald-bearing calcite vein of samples G 67 and G 65. Particularly evident are the perpendicular development of the micas selvages relative to the wall rock and the morphology of calcite in the two samples: fibrous calcite in sample G 67, and rhomboedric calcite in sample G 65.

resenting an earlier stage often reopened and filled with euhedral calcite. Emerald can precipitate in various stages of vein filling, the largest and most beautiful crystals appearing in vugs in the central zone of the veins. K mica identified by SEM analysis is also trapped as solid inclusions within emerald crystals (Fig. 4b).

Sample G 67 (Fig. 3) is a multistage vein characterized by aggregates of K mica on the margin of the vein, fibrous calcite toward the center, locally separated from the 001 K mica planes by aggregates of quartz and albite, and in places interlayered within the mica band. Some quartz crystals may contain small (<0.5 mm) calcite inclusions (Fig. 5). The more central zone of rhombohedral calcite is not shown in Figure 3, but bending of the earlier fibrous calcite and associated K mica due to subsequent strike-slip movements accompanying the development of the later euhedral calcite stage is apparent. Sample G 65 is a single-stage vein consisting of 001 K mica planes developed perpendicular to the vein-wall rock contact as in sample G 67, followed by precipitation of euhedral calcite, pyrite, quartz, REE dolomite, and microgeodic chlorite rosettes (Fig. 3). Microprobe analysis of chlorite indicates a donbassite composition (Merceron et al., 1988) as shown in Table 1.

Composition of K mica aggregates: The chemical composition of the K mica aggregates (Table 1) has been determined by a comprehensive study using electron microprobe, ion microprobe, wet chemical analysis, atomic absorption, and in situ X-ray diffraction.

The major element composition deduced from electron microprobe analysis of the two samples (Table 1) reveals a rather uniform chemical composition. When compared with a standard muscovite analysis (Deer et al., 1962), the average electron microprobe values for sample G 67 (Table 1) yield a normal SiO_2 content (47.68%), a high Al_2O_3 content (36.37%), and a characteristic depletion in K_2O (6.88%) which lead to an apparent excess in octahedral occupancy (4.19; Table 2) and a deficit in the interlayered charge (1.27). Electron microprobe analysis of the sample G 65 (Table 1) reveals the presence of two

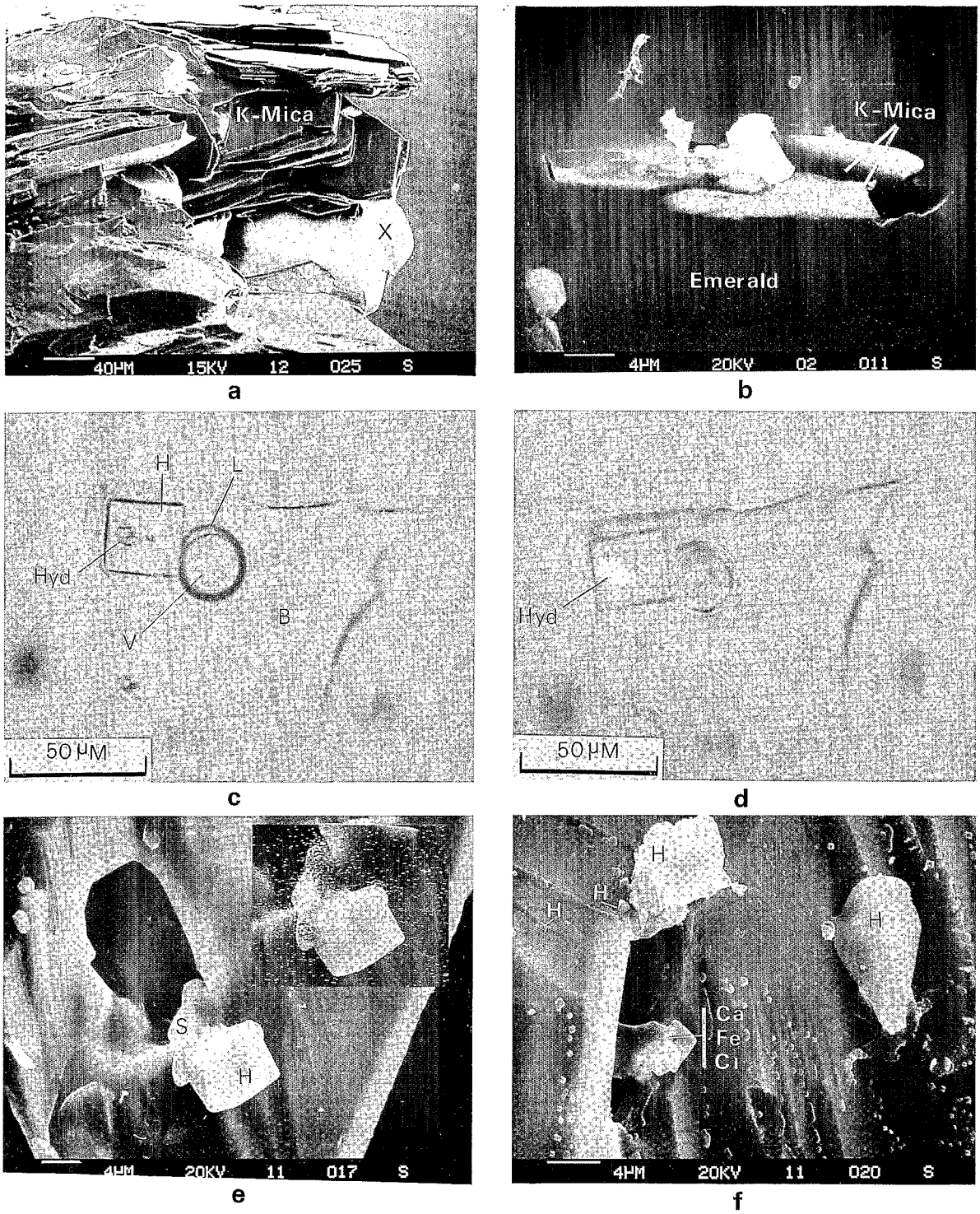

FIG. 4. a. SEM microphotograph of K mica found in a calcite vein; "X" corresponds to an unanalyzed mineral, probably calcite or quartz. Coscuez deposit. b. K mica trapped as solid inclusions in emerald around which developed a fluid inclusion cavity. c. Multiphase fluid inclusion in Coscuez emerald. B = brine, V = vapor phase, L = liquid CO_2; H = halite crystal; Hyd = metastable hydrate nucleated during freezing experiments. d. Same as (c) in crossed polars showing the anisotropic hydrate (Hyd). e. SEM microphotograph of halite (H) and sylvite (S) in an opened fluid inclusion cavity from a Coscuez emerald. The upper right shows the backscattered K electron image of the same salt (scanning time: 400 sec). f. SEM microphotograph of decrepitates of a brine-bearing fluid inclusion. H = halite; Ca, Fe, Cl = salt mixture of calcium, iron, and chlorine.

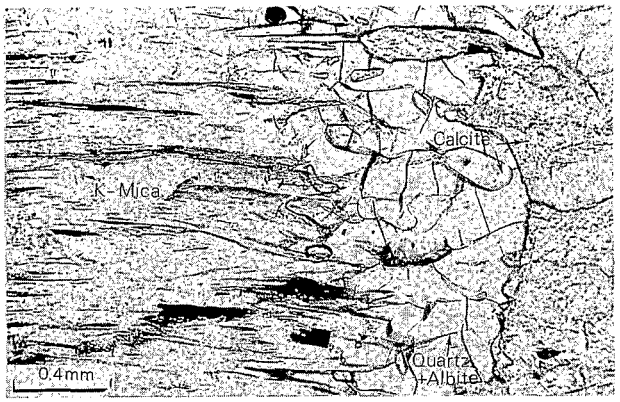

FIG. 5. Quartz-albite intergrowth with minute calcite inclusions characterizing the K mica-fibrous calcite transition in the Coscuez emerald veins.

interlayered micaceous phases within the K mica bands that are optically indistinguishable. The more representative phase of G 65 appears similar to G 67 (SiO_2 = 45.40%, Al_2O_3 = 36.78%, K_2O = 6.70%; analysis for G 65(1), Table 1). Apparent excess in octahedra occupancy (4.19; Table 2) and deficit in the interlayered charge (1.37) are also noticeable. The other phase is an Na-bearing phyllosilicate where Na_2O replaces K_2O, compared with the previous analysis (Na_2O = 5.09%, K_2O = 2.0%; G 65(2) analysis, Table 1). This phase appears chemically equivalent to a paragonitic substitution of muscovite. According to Deer et al. (1962), the G 65(2) microprobe analysis is comparable to a sodium-illite (or brammalite) composition.

Complementary in situ ion microprobe analysis on the G 67 sample (Table 1) shows low contents of Li_2O = 0.054 percent, F = 0.18 percent, and Be = 3.2 ppm. Atomic absorption analysis yields high contents of Cr (208 ppm) and V (892 ppm) that are, as for emerald, responsible for the green color of the K mica. High H_2O contents, compared with standard muscovites, are revealed by in situ ion microprobe analysis (5.5%; Table 1), cross-checked by chemical volumetric analysis done on whole-rock aggregates (6.11%; Table 1). A reconstituted analysis incorporating the 15 elements analyzed by the different techniques (total = 99.21%) is proposed in Table 1 for sample G 67; it displays a good concordance with a

TABLE 1. Major and Trace Element Analyses of Sheet Silicates Used for $^{40}Ar/^{39}Ar$ Analysis, Quipama (G 65) and Coscuez (G 67) mines, Colombia

Sample	G 65(1)		G 65(2)		G 67		G 67 (3, 4, and 5)			G 67		Hydromuscovite (6)	G 65	
Method	Electron microprobe		Electron microprobe		Electron microprobe		Multitechnique analysis			Reconstituted analysis			Electron microprobe donbassite	
	n = 7		n = 3		n = 9								n = 3	
	wt %	σ	wt %	σ	wt %	σ		G 67 (3)					wt %	σ
SiO_2	45.40	0.53	47.50	0.85	47.68	0.47	Li_2O	0.054%		SiO_2	47.68	47.55	36.61	0.78
TiO_2	0.09	0.06	0.006	0.004	0.13	0.05	F	0.18%		TiO_2	0.13	0.64	0.00	
Al_2O_3	36.78	0.34	38.29	0.17	36.37	0.70	Be	3.2 ppm		Al_2O_3	36.37	32.45	45.73	1.62
MgO	0.33	0.04	0.075	0.016	0.79	0.19	B	traces		MgO	0.79	1.70	0.04	0.04
CaO	0.007	0.01	0.14	0.03	0.006	0.01	Cl	traces		CaO	0.006	0.06	0.15	0.03
MnO	0.023	0.03	0.02	0.013	0.015	0.02	H_2O	5.5		MnO	0.015	0.00	0.04	0.03
FeO	0.24	0.11	0.07	0.02	0.19	0.09				FeO	0.19	0.85	0.00	
Na_2O	0.80	0.43	5.09	0.30	0.41	0.07		G 67(4)		Na_2O	0.41	1.05	0.05	0.03
K_2O	6.70	0.47	2.00	0.40	6.88	0.49		wt %	σ	K_2O	6.88	6.22	0.05	0.02
Rb_2O	0.045	0.04	0.037	0.013	0.025	0.02				Rb_2O	0.025		0.02	0.01
F	0		0		0.024	0.03	H_2O	6.11	0.045	F	0.18			
Total	90.42		93.23		92.52					Li_2O	0.054			
								G 67 (5)		V_2O_5	0.16			
										Cr_2O_3	0.03			
							Cr	208 ppm		H_2O	6.11	7.73		
							V	892 ppm						
							Be	2.4 ppm		Total	99.21	100.01	82.89	

Microprobe analysis carried out at the Camebax electron microprobe (University of Nancy I, France). Analytical conditions: acceleration voltage, 15 KV; sample current, 6-8 nA; silicate crystals as standards; and ZAF correction procedure; n = number of points used to calculate an average analysis; σ = standard deviation; Samples: (1) and (2), respectively, the K- and Na-bearing micas of the emerald veins in sample G 65, (3), ion microprobe analysis of sample G 67 (two points) using a modified CRPG ion microprobe Cameca IMS 3F; quantitative estimation is made by normalization to the SiO_2 = 47.68 avg wt % from the electron microprobe analysis and by reference to a standard lepidolite; (4), measurement done by the Karl Fischer volumetric method; (5), atomic absorption analysis; (6), chemical analysis of hydromuscovite from Deer et al. (1962)

TABLE 2. Structural Formulas of K Micas Based on Electron Microprobe Analyses in Table 1 (calculation based on 22 oxygens)

Sample	G 65(1)	G 65(2)	G 67
Si	6.18	6.17	6.32
Al	5.90	5.87	5.68
Fe^{2+}	0.03	0.01	0.02
Mg	0.07	0.01	0.16
Ti	0.01	0.00	0.01
Mn	0.00	0.00	0.00
Ca	0.00	0.02	0.00
Na	0.21	1.28	0.11
K	1.16	0.33	1.16
Total Y	4.19	4.06	4.19
Total X	1.37	1.63	1.27

hydromuscovite analysis from Deer et al. (1962) in which the increase in H_2O content relative to a standard muscovite is interpreted as reflecting the substitution of H_3O^+ for K^+ (Brindley, 1980).

Routine X-ray powder analyses of the mica aggregates display a single muscovite $2M_1$ structure for sample G 67 and a dominant muscovite $2M_1$ polymorph structure for sample G 65 added to a strong reflection at 14 Å which could represent some donbassite contamination of the K mica aggregate (see above). More careful examination using in situ X-ray diffraction identification on petrographic thin sections (Beaufort et al., 1983; Rassineux et al., 1987), revealed the presence of minor amounts of paragonite (9.6 Å) and kaolinite (7.16 Å) in addition to muscovite (10 Å). However, kaolinite is not always present. A spectrum of Quipama sample G 65, choosen among ten points analyzed by XRD on a thin section of the mica aggregate, is presented in Figure 6.

Therefore, the reconstructed hydromuscovite chemical analysis deduced from electron microprobe and ion microprobe analysis can be reinterpreted considering the XRD data, using a simple melange model of pure muscovite and kaolinite phases, the muscovite being, by far, the most abundant (80–90 vol % as deduced from the respective intensity of the XRD peaks). Indeed, bulk electron microprobe analysis of a fine muscovite-kaolinite mixture will result in some Al_2O_3 increase, thus giving an apparent excess in the octahedral occupancy relative to a standard muscovite. In addition, this kaolinite contamination will also result in some apparent increase in H_2O and decrease in K_2O relative to a pure muscovite phase.

Analytical procedure for $^{40}Ar/^{39}Ar$ analyses

Due to the clay-size imbrication of muscovite and kaolinite of the Colombian emerald-bearing vein, not even visible by means of SEM observation (Fig. 4a), it was impossible to obtain pure concentrates of muscovite. Therefore, the K mica aggregates used for $^{40}Ar/^{39}Ar$ dating purposes were simply hand-separated by using a fine saw. No special treatment was applied thereafter.

Three complementary $^{40}Ar/^{39}Ar$ procedures were adopted: (1) an induction step-heating procedure performed on bulk samples of K mica aggregate (described in Féraud et al., 1982, 1986) (2) a laser spot fusion procedure on K mica aggregates or on fragmented K mica band slabs, and (3) laser step-heating experiments on K mica aggregates.

Bulk samples were obtained by handpicking aggregates of green micas to be as pure as possible. Step-heating experiments were performed on bulk samples and single grains of mica aggregates consisting of 2-mm-diam clusters of adjacent mica flakes. Spot fusion analyses were performed on slabs obtained by microsawing of the mica coating parallel to the vein. The G 67 slab (Fig. 3) is 1.4 mm thick and consists of a 0.5-mm-thick K mica band plus a 0.9-mm-thick adjacent band composed of a mixture of K mica, quartz, albite, and calcite. The G 65 slab is composed of a single 0.9-mm-thick single K mica band (Fig. 3). Laser spot fusion analyses were also performed on

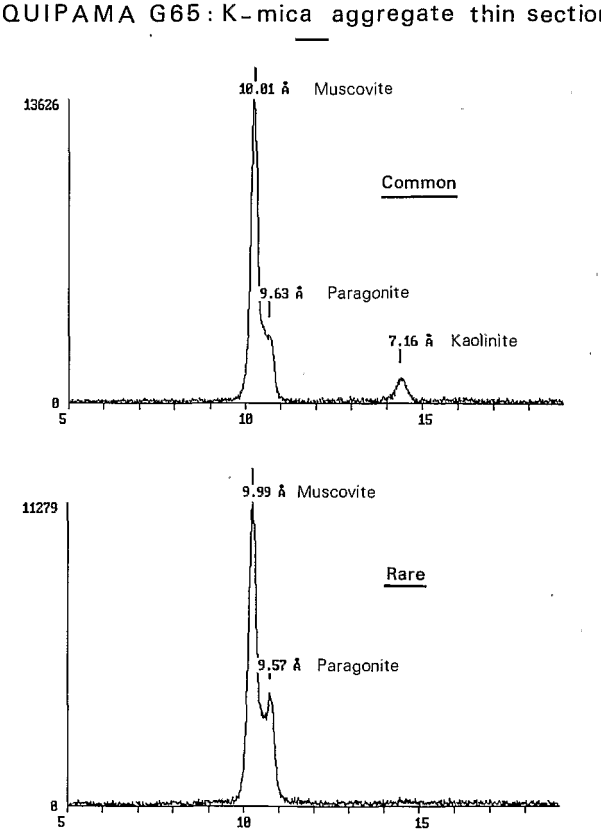

FIG. 6. Diffraction pattern of sample G 65 obtained by XRD on a thin section using a step-scanning method and a linear localization detector (Beaufort et al., 1983).

one G 65 mica aggregate and the G 67 K mica band perpendicular to the wall-rock plane.

The laser microprobe device and procedure of the University of Nice (France) is decribed in Scaillet et al. (1990) and Ruffet et al. (1991). The selected mica separates and rock slabs were irradiated for 14.3 hr in the Osiris reactor (CEN, Saclay) with the biotite Bern 4B (17.25 Ma, Hall et al., 1984, and subsequent analyses) as monitor. The isotope correction procedures and the criteria used to define plateau age are given in Féraud et al. (1986). All ages have been calculated with the decay constants recommended by Steiger and Jäger (1977) and are given with standard error (1 σ) estimates. Analytical data are presented in Tables 3 and 4.

$^{40}Ar/^{39}Ar$ dating results

Step-heating experiments: Bulk samples and single grain aggregates of the two samples show similar age spectra, characterized by increasing ages at low temperature, followed by decreasing ages, then a more or less flat domain. Sample G 65 (Fig. 7) yields a plateau age at 31.5 ± 0.3 Ma (corresponding to 82% of ^{39}Ar released) on a single grain aggregate, whereas the corresponding bulk sample displays more precise concordant ages with an integrated value of 32.6 ± 0.1 Ma (over 60% of ^{39}Ar released). Sample G 67 does not give any plateau age over a high percentage of the ^{39}Ar released (Fig. 8), but except for the low-temperature domain, it displays no more variable ages than does G 65. However, most of the apparent ages for this sample range from 35 to 38 Ma.

Spot fusion experiments: In order to examine a possible variation of the integrated ages from the wall-rock side of the vein toward its center, several laser spot experiments have been performed on the two slab sections across the K mica layers. For sample G 67, the ages range from 34 ± 2 to 38.9 ± 1 Ma without any correlation between ages and distances to the outer rim of the K mica band (Table 3, Fig. 9). The weighted mean of 36.8 ± 0.4 Ma is close to integrated ages of both the bulk sample (i.e., 37.3 ± 0.1 Ma) and the single grain aggregate (i.e., 36.4 ± 0.1 Ma). The corresponding ($^{37}Ar_{Ca}/^{39}Ar_K$) ratios range from 0.004 to 0.48. Three older ages from 52 to 130 Ma were obtained by spot fusion analysis performed on the inner mixed zone adjacent to the mica band (Fig. 9). The corresponding ($^{37}Ar_{Ca}/^{39}Ar_K$) ratios range from 55 to 174 (Table 3). Additional laser spot fusion experiments have been performed perpendicular to the wall-rock plane of the slab (36.2 ± 0.4 Ma) and on an isolated mica aggregate (36.4 ± 0.1 Ma) which was completely fused in one step. For sample G 65, four spot fusion analyses performed on the K mica slab (Fig. 9) give similar ages, ranging from 30.1 ± 0.8 to 33 ± 2 Ma (Table 4), whereas an older age of 39.8 ± 1.1 Ma was obtained on the external border at the wall-rock face of the slab. Their weighted mean of 32.8 ± 0.4 Ma is close to the integrated ages of 33.1 ± 0.1 and 31.4 ± 0.3 Ma on the bulk sample and single grain aggregate, respectively (Table 4). The ($^{37}Ar_{Ca}/^{39}Ar_K$) ratios range from 0.0056 to 0.130 which represents a lower scale than that of sample G 67. Two spot fusions performed on the inner and outer faces of one isolated fragment of the mica slab (Fig. 9) display similar ages of 31.8 ± 0.2 and 32.1 ± 0.5 Ma, whereas the ($^{37}Ar_{Ca}/^{39}Ar_K$) ratios range from 0.045 to 0.0055.

Discussion of $^{40}Ar/^{39}Ar$ results

On both samples, we observe good agreement between the integrated ages of the step-heating experiments on bulk samples and single mica aggregates as well as agreement between the weighted means of the spot fusion analyses, if we except some spot fusion ages which appear significantly higher. Nevertheless, these ages were obtained from peculiar locations on the slabs. Point 2 of sample G 65 (Fig. 9, Table 4) is located on the wall-rock side and may be affected by contamination with the Cretaceous black shale. Points 3, 11, and 15 of G 67 (Fig. 9, Table 3) were performed on the pure K mica vein. The argon released may have originated, as demonstrated by higher $^{37}Ar_{Ca}/^{39}Ar_K$ ratios, from a mixture of K mica with other minerals (quartz-albite-calcite) containing fluids in inclusions and therefore some possible amounts of excess argon.

In spite of the existence of one plateau age (G 65), the age spectra of both samples (a bulk sample and single grains) are affected by slight disturbances which are not clearly related to the $^{37}Ar_{Ca}/^{39}Ar_K$ ratio (Figs. 7 and 8). Some inverse correlation may appear at low temperature, the highest values of the $^{37}Ar_{Ca}/^{39}Ar_K$ ratio being due to calcite impurities degassing. On the other hand, no age disturbance corresponds to a clear increase of the $^{37}Ar_{Ca}/^{39}Ar_K$ ratio at high temperature (G 67, Fig. 8). This peak may be induced by the degassing of minute calcite inclusions in quartz crystals as observed in thin sections (Fig. 5).

The reproducible shape of the age spectra, characterized by increasing ages followed by a saddle shape, may be explained by the degassing of different mineral phases during step heating or/and ^{39}Ar recoil during the irradiation. These age spectra are very similar to those obtained on chloritized biotites (Lo and Onstott, 1989) which were interpreted as resulting from ^{39}Ar recoil from biotite to chlorite layers. Recoil of ^{39}Ar can potentially explain the disturbances observed in the age spectra because the thickness of the individual mica crystals (1–3 μm; Fig. 4a) is not very large compared to the accepted ^{39}Ar recoil distance (0.08 μm; Turner and Cadogan, 1974). Nevertheless, in the case of homogeneous aggregates of small micas, any eventual ^{39}Ar recoil may not induce argon

TABLE 3. $^{40}Ar/^{39}Ar$ Analytical Data for Sample G 67 (Coscuez Mine)

	Atmospheric contamination (%)	^{39}Ar (%)	$^{37}Ar_{Ca}/^{39}Ar_K$	$^{40}Ar_{radiogenic}/^{39}Ar_K$	Apparent age (Ma)	Error ±1 σ
Bulk sample induction furnace analysis Temperature (°C)						
500	97.13	0.33	0.0209	0.70956	16.01	±7.76
550	82.3	0.72	0.02033	1.1551	25.98	±3.23
600	62.72	1.5	0.05995	1.3707	30.79	±1.64
650	35.56	5.11	0.28399	1.4718	33.04	±0.5
700	26.13	10.07	0.07658	1.6011	35.92	±0.26
730	15.72	10.97	0.00392	1.6984	38.08	±0.25
760	6.48	31.27	0.00150	1.6977	38.06	±0.12
790	10.63	15.47	0.00163	1.6655	37.35	±0.17
830	21.65	6.1	0.00778	1.6482	36.96	±0.39
880	38.27	2.71	0.00873	1.6757	37.57	±0.87
970	33.04	3.92	0.00898	1.6951	38	±0.66
1,030	28.11	5.25	0.00471	1.7183	38.52	±0.49
1,150	24.7	6.53	0.00462	1.7279	38.73	±0.39
Fuse	93.3	0.04	0.85166	17.66	361.39	±53.34
					Integrated age = 37.3 ± 0.1	
Single grain laser analysis Steps						
1	63.07	0.04	0.0	2.6797	59.72	±46.35
2	71.52	0.2	0.0	1.2469	28.03	±12.81
3	24.7	1.0	0.02469	1.2333	27.73	±2.19
4	5.36	1.5	0.1174	1.4272	32.05	±1.11
5	8.12	5.49	0.04266	1.5664	35.15	±0.48
6	1.79	23.04	0.00335	1.684	37.76	±0.13
7	1.65	11.7	0.00256	1.6284	36.52	±0.25
8	3.21	7.44	0.00223	1.5905	35.68	±0.41
9	3.54	9.02	0.00247	1.5838	35.53	±0.3
10	2.21	3.46	0.00102	1.5958	35.8	±0.57
11	2.96	2.31	0.00137	1.5934	35.75	±0.9
12	2.77	4.41	0.00181	1.6106	36.13	±0.5
13	2.3	8.29	0.00298	1.6454	36.9	±0.35
14	12.87	5.3	0.00695	1.645	36.89	±0.46
15	25.86	2.27	0.03458	1.5614	35.03	±1.1
16	2.99	14.54	0.00521	1.6433	36.85	±0.24
					Integrated age = 36.4 ± 0.1	
Single grain total fusion	2.42		0.0511	1.6248	36.44	±0.14
Slab spot fusion (transversal plane) Spot number (see Fig. 10)						
1	14.59		0.11386	1.5721	35.27	±1.13
2	55.88		0.04851	1.5986	35.86	±4.12
4	50.41		0.04192	1.618	36.29	±6.05
5	41.73		0.22498	1.7366	38.92	±1.06
6	39.99		0.47792	1.6984	38.08	±0.92
7	22.02		0.05297	1.5564	34.92	±0.93
8	14.6		0.01316	1.5145	33.99	±2.45
9	10.95		0.00565	1.6944	37.99	±0.99
10	10.19		0.00431	1.6052	36.01	±1.2
					Weighted mean = 36.8 ± 0.4	
3	84.74		54.693	2.3374	52.2	±7.4
11	65.91		173.55	5.9665	130.36	±14.98
15	54.92		105.49	2.4746	55.2	±10.9
Slab spot fusion (longitudinal plane)	37.95		0.34698	1.6125	36.17	±0.39

TABLE 4. $^{40}Ar/^{39}Ar$ Analytical Data for Sample G 65 (Quipama Mine)

	Atmospheric contamination (%)	^{39}Ar (%)	$^{37}Ar_{Ca}/^{39}Ar_K$	$^{40}Ar_{radiogenic}/^{39}Ar_K$	Apparent age (Ma)	Error ±1 σ
Bulk sample induction furnace analysis						
Temperature (°C)						
400	98.58	0.2	0.02204	0.79887	18.01	±10.82
470	94.46	0.34	0.01778	0.92996	20.95	±5.64
520	81.56	0.99	0.01428	1.2567	28.25	±1.9
570	72.16	2.54	0.01891	1.3534	30.41	±0.82
620	57.96	5.64	0.06035	1.4112	31.69	±0.38
660	45.31	7.33	0.07626	1.4771	33.16	±0.28
690	29.07	10.15	0.02532	1.5567	34.93	±0.3
720	31.17	8.16	0.00949	1.5236	34.19	±0.28
770	19.36	17.15	0.00433	1.4492	32.54	±0.13
785	21.8	11.12	0.00217	1.4625	32.84	±0.19
810	36.17	3.43	0.00460	1.4765	33.15	±0.54
840	30.65	5.57	0.00306	1.4485	32.52	±0.37
880	33.89	4.9	0.00328	1.4355	32.23	±0.39
920	35.98	4.07	0.00341	1.4557	32.68	±0.47
970	42.09	3.13	0.00363	1.4689	32.98	±0.58
1,030	19.5	11.28	0.00212	1.4511	32.58	±0.19
1,110	41.55	3.76	0.00855	1.5735	35.3	±0.5
1,190	94.17	0.09	0.06302	3.2846	72.93	±19.41
Fuse	92.77	0.16	0.04135	4.651	102.42	±13.04
				Integrated age = 33.1 ± 0.1		
Single grain laser analysis						
Steps						
1	100	0.17	0.01016	0.62442		±
2	87.98	0.71	0.0137	0.35887	8.11	±11.24
3	23.41	2.99	0.02701	1.3056	29.34	±2.57
4	13.84	6.52	0.01962	1.3612	30.58	±1.39
5	7.82	7.7	0.01104	1.5243	34.21	±0.93
6	8.79	13.08	0.00704	1.4556	32.68	±0.8
7	8.82	22.58	0.00343	1.3689	30.75	±0.42
8	4.39	18.43	0.00286	1.3925	31.28	±0.47
9	8.99	5.39	0.00284	1.319	29.64	±1.3
10	4.25	7.02	0.00296	1.3801	31	±1.35
11	2.15	11.3	0.00402	1.457	32.71	±0.76
12	9.92	4.1	0.00964	1.4919	33.49	±2.11
				Integrated age = 31.4 ± 0.3		
Slab spot fusion						
Spot number (see Fig. 10)						
1	44.13		0.06212	1.4532	32.63	±0.61
2	31.21		0.01226	1.7772	39.82	±1.14
3	16.02		0.05636	1.4061	31.58	±1.04
4	27.7		0.13017	1.3406	30.12	±0.83
5	22.8		0.02067	1.4667	32.93	±1.58
				Weighted mean = 32.8 ± 0.4		
6	21.84		0.04471	1.4154	31.79	±0.24
7	9.26		0.00553	1.431	32.13	±0.51
				Weighted mean = 31.9 ± 0.2		
8	44.13	100	0.6212	1.4532	32.63	±0.61

loss because the recoiled ^{39}Ar has a high probability of being implanted within a neighboring crystal (Bray et al., 1987). In our case, the recoiled ^{39}Ar may have been introduced into minor amounts of kaolinite, chlorite, or paragonite interlayered within the K mica aggregates. Therefore, the humped shape around the 690°C step of the G 65 bulk sample age spectrum (Fig. 7) may be due to a deficiency of ^{39}Ar

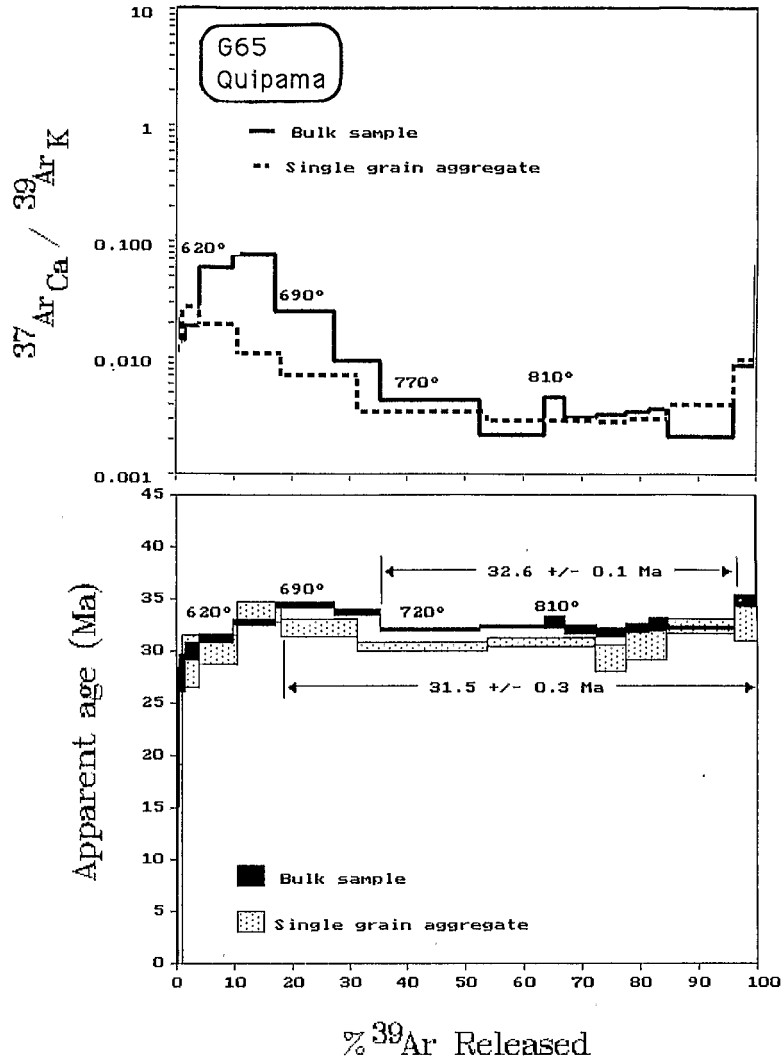

FIG. 7. Induction (bulk sample) and continuous laser microprobe step-heating (single grain aggregate) age and ($^{37}Ar_{Ca}/^{39}Ar_K$) ratio spectra of sample G 65.

in the muscovite K-rich phase, whereas the low ages displayed at lower temperatures may originate from a gain of ^{39}Ar in the K-poor phases. This is supported by the fact that the integrated age of these two domains of the age spectrum (steps 400°–720°C) is 33.1 ± 0.2 Ma, similar to that of the plateau age, 32.6 ± 0.1 Ma. The absence of ^{39}Ar loss on chloritized biotites affected by ^{39}Ar recoil was demonstrated by Ruffet et al. (1991). To test a hypothetical ^{39}Ar loss, a conventional K-Ar experiment was performed on sample G 65 at the CRPG-CNRS laboratory of Nancy, France (see Zimmermann et al., 1985, for the general procedure). An age of 32.8 ± 3.9 Ma ($^{40}Ar = 6.55 \times 10^{-6}$ cc/g; ^{40}Ar atm = 91.3%) similar to the $^{40}Ar/^{39}Ar$ ages was obtained and thus precludes a high amount of ^{39}Ar loss by recoil in that sample.

The disturbance of the age spectra may be explained by the existence of a mixture of different K-bearing mineral phases, characterized by distinct $^{40}Ar_{radiogenic}/^{39}Ar_K$ ratios, degassing at different temperatures. Paragonite and kaolinite were detected by optical microprobe analysis, but in very different proportions in the two samples G 65 and G 67. Nevertheless, because of the reproducibility of the $^{40}Ar/^{39}Ar$ results, whatever the technique and the volume of analyzed samples, it is unlikely that these mineral heterogeneities are sufficient to explain the observed phenomena without a contribution of ^{39}Ar recoil.

Regardless of slight disturbances due to probable internal Ar recoil evidenced by laser step-heating and laser spot experiments, it is likely that the ages of 31.5 to 32.6 Ma (sample G 65) and 35 to 38 Ma (sam-

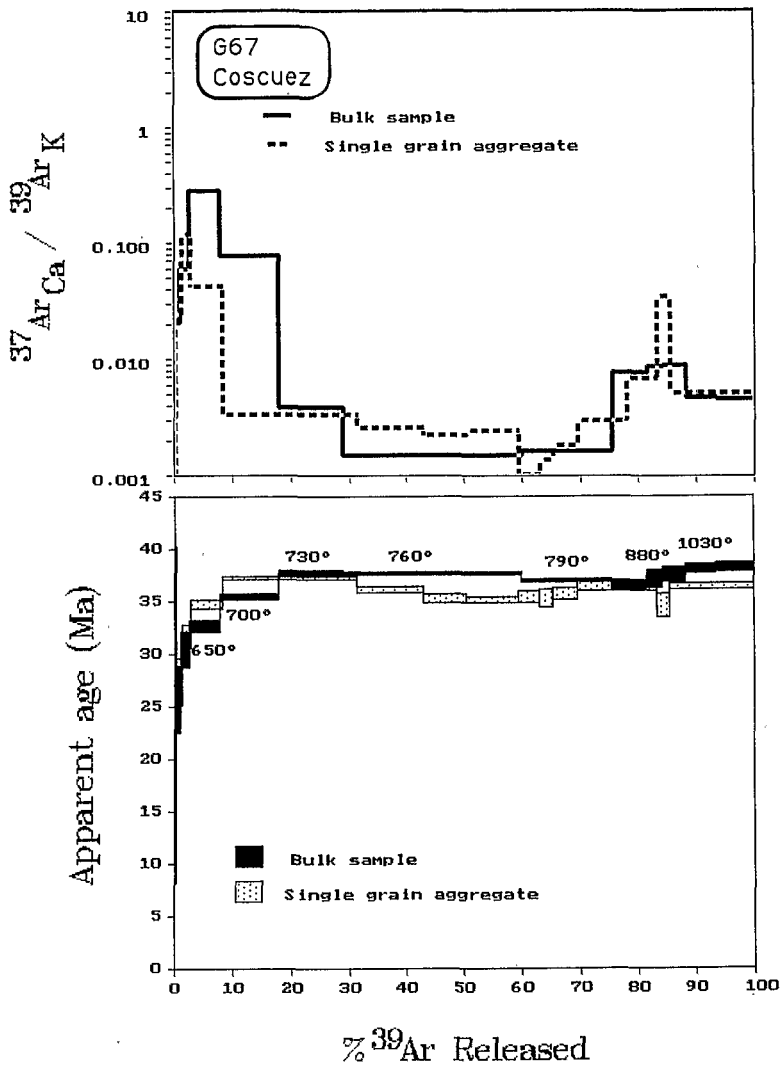

FIG. 8. Induction (bulk sample) and continuous laser microprobe step-heating (single grain aggregate) age and ($^{37}Ar_{Ca}/^{39}Ar_K$) ratio spectra of sample G 67.

ple G 67) represent reasonable estimates of the age of the muscovite synchronous with the emerald deposition. The age difference between samples from the two locations is probably real. These results give an unambiguous late Eocene to lower Oligocene age (Odin and Montanari,1989) for the Colombian emerald deposits.

Fluid Inclusion Study

Introduction

The first extensive work on fluid inclusions of Colombian emeralds was performed on samples from the Achiote deposit (eastern belt) by Kozlowski et al. (1988). Heating experiments were problematic due to common decrepitation, stretching, and subtle leaking of fluid inclusions. The temperatures of homogenization (T_h) by vapor disappearance were near 470°C and fluid inclusions with $T_h > 470$°C were suspected of leaking. Using decrepitation temperatures in quartz and beryl, Kozlowski et al. (1988) gave a rough pressure estimate of formation of 1 kbar which yields an additional pressure correction of 100°C for the T_h values. The trapping temperature estimated by Roedder (1982, 1984) was $T_{trapping} >$ 518°C, and Ottaway and Wicks (1986) noted a total homogenization by NaCl dissolution at 320° ± 10°C for the Muzo deposit.

Analytical methods

The microthermometric study was performed on doubly polished plates using a microscope equiped

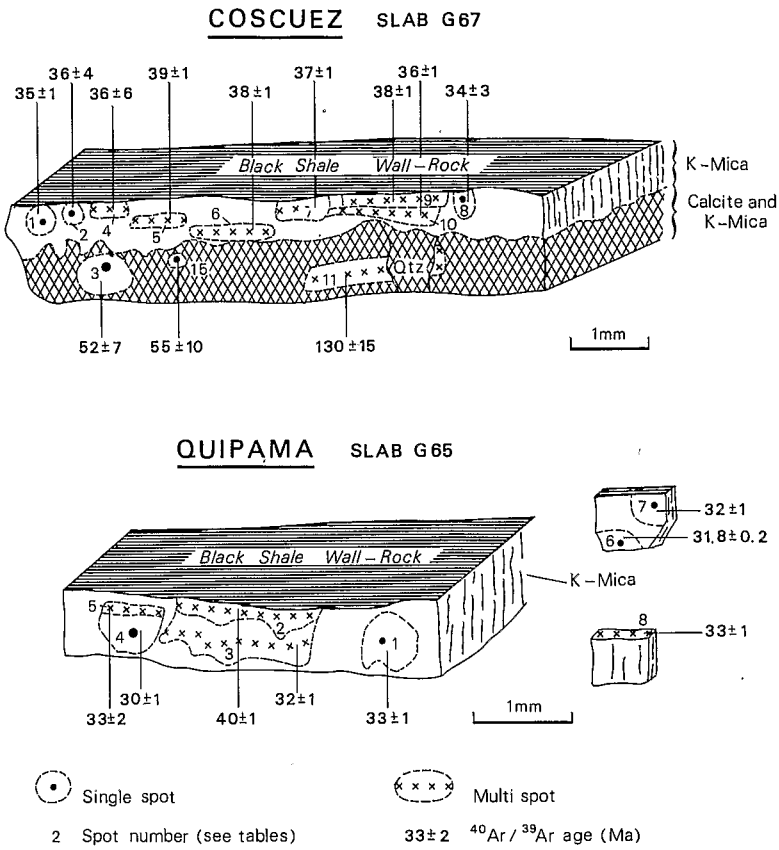

FIG. 9. Position of the laser spot fusion analysis on the slab samples.

with a UMK 50 Leitz objective and a Chaixmeca heating-freezing stage (Poty et al., 1976). The low-temperature measurements were obtained with a precision of 0.1°C; the high-temperature measurements were made by heating the inclusions at a rate of 1°C per min. Raman spectra of hydrates, volatile components of the vapor phase, and solid daughter minerals were obtained on a Dilor X-Y multichannel laser-excited Raman spectrometer using the 514.5-nm radiation of an Ar ion laser (Dubessy et al., 1989). The presence of the volatile components CO_2, CH_4, N_2, and H_2S was checked using a 1-W laser beam referring to the following lines, respectively: 1.388 cm^{-1}, 2.915 cm^{-1}, 2.331 cm^{-1}, and 2.611 cm^{-1}. SEM examination was performed with a Cambridge Stereoscan 250 SEM operating at an accelerating voltage of 25 kV.

Fluid inclusion petrography

Primary and secondary fluid inclusions in emerald are typically brines (Fig. 4c and d). At room temperature, the degree of filling of the cavities is fairly constant. The inclusions typically contain a cubic crystal of halite (12–15 vol %), a brine (75 vol %), a vapor bubble (10 vol %), and a liquid carbonic phase ($CO_{2(l)}$) which is easily visible in flat and large inclusions. This carbonic phase constitutes up to 3 percent of the total cavity volume (Fig. 4c and d). The halite-bearing fluid inclusions may contain a variety of additional daughter minerals which were investigated by SEM. The association NaCl-KCl is common in Coscuez emeralds (Fig. 4e) and different salt mixtures were identified in decrepitates: Cl(Ca, Fe) salts (Fig. 4f), Cl(Fe, K, Ca), Cl(Fe, Mn, Ca, K), and Cl(K, Fe). Other daughter minerals include Ca + Fe ± Mn ± Mg carbonates with rhombohedral habit, Zn sulfide, and Fe oxide.

Freezing experiments

Carbon dioxide was identified by $T_{m_{CO_2}}$ (CO_2 final melting temperature), $T_{h_{CO_2}}$ (CO_2 homogenization temperature), CO_2 gas hydrate final melting temperature or by Raman analysis of the vapor phase. The $T_{m_{CO_2}}$ values range from −56.6° to −57.9 °C (Fig. 10) which confirms the presence of N_2, as identified by its 2,330 cm^{-1} Raman peak.

During microthermometric runs, fluid inclusions exhibited a characteristic behavior: the ice begins to melt between −50.5 and −59.5°C (Fig. 10) and the final melting temperature of ice ($T_{m_{ice}}$) ranges from

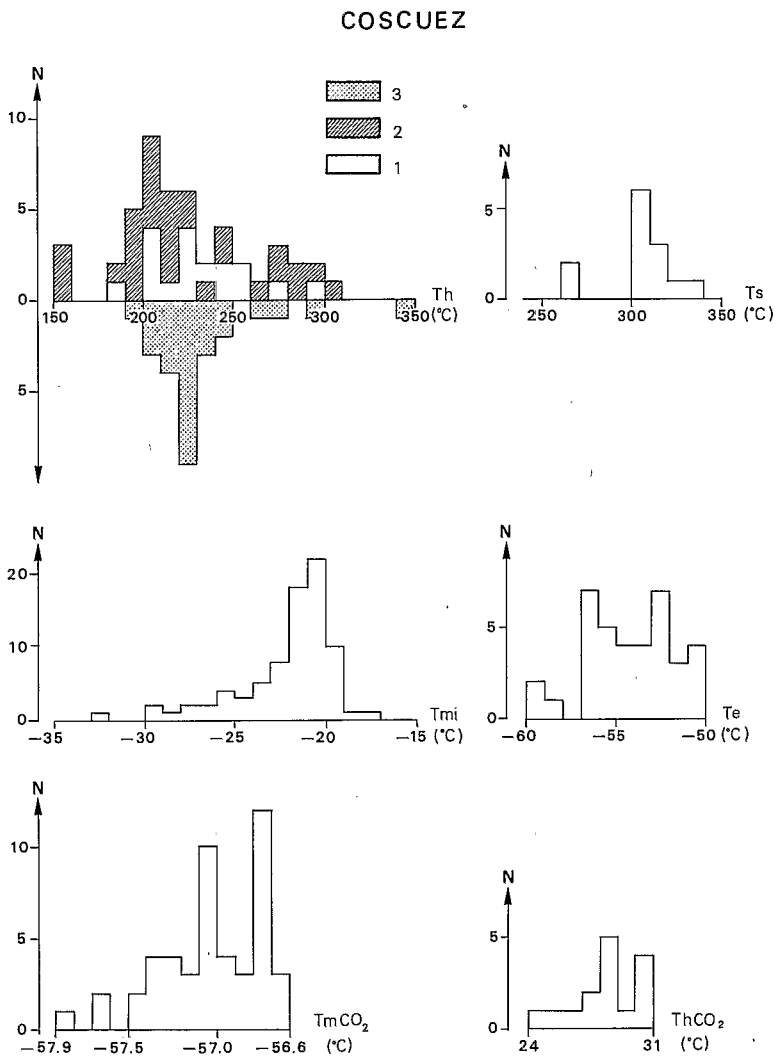

FIG. 10. Histograms of microthermometric data for primary fluid inclusions from Coscuez emeralds. Th = temperature of homogenization of the vapor bubble; 1 = complete homogenization; 2 = leakage before homogenization; 3 = decrepitation before homogenization. Ts = halite dissolution temperature. Tmi = ice melting temperature. Te = eutectic temperature. $TmCO_2$ = CO_2 melting temperature. $ThCO_2$ = CO_2 homogenization temperature.

−32.3° to −17.6°C. The $T_{m_{clathrate}}$ range from −25.1° to −19.3°C. In some large fluid inclusions, the brine exhibited a delayed freezing upon supercooling of long duration down to −180°C which might be due to the high salinity and viscosity of the fluid as described by Roedder (1963) and Kozlowski et al. (1988) for the Achiote deposit. Moreover, Kozlowski et al. (1988) documented the chemical components of the hydrothermal brines by SEM analyses of the decrepitates; they found decreasing concentrations of Cl, Na > Ca, Si, Al > Fe, K, Mg > Mn, and Ti and interpreted the inability of the fluid to freeze as being the result of Ca and Al ions on the nucleation of solid phases at low temperature.

The low eutectic temperatures (−50° to −60°C) and the final melting of ice ($T_{m_{ice}}$ = −17° to −33°C; mode −21°C; Fig. 10) confirm that the trapped solutions contain significant amounts of $CaCl_2$ (Crawford, 1981). The existence of other ions in the brine is suggested by the SEM analyses of daughter minerals and the nucleation of new daughter minerals during supercooling. These solids, which grew on NaCl daughter minerals, have been described by Roedder (1963) and Touray and Poirot (1968). They are anisotropic and possess a moderate relief (Fig. 4c and d). On heating, they persist until melting over a range of 4.4° to 141°C. Therefore, these solids are probably hydrates. Raman spectrometry characterizes their

peaks at 3,416, 1,653, and 1,634 cm^1 (Giuliani et al., 1993) which are typical of known hydrates (Dubessy et al., 1989). However, the exact identification of these phases is not possible, considering the lack of precise spectra for hydrates of geologic interest.

Heating experiments

On heating, liquid CO_2 homogenizes to vapor in the range 24.3° to 30.9°C (Fig. 10). This corresponds to a low-density CO_2 phase (ρ = 0.2–0.4 g/cm^3). Decrepitation and leakage occurred in a majority of fluid inclusions, especially those >20 μm in size. Leakage was often marked by "a sudden reversal in the gradually diminishing size of the bubble as temperatures increased" (Roedder, 1982, p. 498) and the larger inclusions generally exploded. When no leakage phenomenon occurred, a characteristic behavior of inclusions during heating was observed. Under increasing heating (T_h scattered between 180° and 190°C), halite becomes more rounded, the vapor bubble decreases in size, and finally disappears leaving liquid and halite; under further heating, final halite dissolution temperature (T_s) ranges between 260° and 340°C, with a representative mode at 305°C (Fig. 10).

Bulk salinity estimation

The microthermometric and SEM data demonstrate the presence of Ca^{2+} ions in the brines. The presence of CO_2, N_2, and in some cases, KCl has also been demonstrated. Such complex composition does not allow rigorous use of the experimental data of Vanko et al. (1988) to estimate the bulk composition of these fluids, as done by Giuliani et al. (1993) for CO_2-free brines of the Vega-San Juan mine in the eastern belt (resulting composition = $(H_2O)_{55}$-$(NaCl)_{30}$-$(CaCl_2)_{15}$). However, the lower $T_{m_{ice}}$ values in the Coscuez deposit compared to those of the Vega-San Juan deposit (some values are characteristically below −21.2°C) would indicate a lower content of $CaCl_2$ in the fluid (max 5 mole % determined by extrapolating the ternary diagram data; Vanko et al., 1988). Therefore, we have adopted an estimation of the salinity of the Coscuez fluids based on the simple H_2O-NaCl system (Potter and Brown, 1975) and the halite dissolution temperature ($T_{m_{halite}}$) at 305°C. The data of Hall et al. (1988) yield a global salinity estimate of 38 wt percent NaCl equiv.

Pressure-temperature determination of emerald deposition

Because of the chemical complexity of the fluid inclusions, two representative isochores were constructed (Brown and Lamb, 1989) to bracket the P-T evolution of the ore-forming brines (Fig. 11). The first isochore corresponds to a representative T_h = 235°C and a total salinity of 38 wt percent NaCl equiv. The second is drawn for T_h = 300°C, which represents the highest T_h value for the same total salinity.

The pressure correction has been determined assuming a lithostatic confining pressure. The presence of hydraulic fracturing breccia indicates that during the implosion of black shales, the fluid pressure exceeded the lithostatic pressure ($P_{fluid} \geq P_{solid}$). The stratigraphic column reconstruction of the Eastern Cordillera of Colombia by Hébrard (1985) permits estimation of the depth of overburden at about 4,250 and 4,500 m for ages of 35 and 38 Ma, respectively (Fig. 11), as determined by the $^{40}Ar/^{39}Ar$ study for the Coscuez deposit. Assuming a rock density of 2.5 g/cm^3, this depth corresponds to a lithostatic pressure of 1.06 and 1.12 kbars, respectively. Therefore, as deduced from Figure 11, two effective trapping temperatures can be estimated at $T_{trapping_1}$ = 290°C and $T_{trapping_2}$ = 360°C for the brines responsible for the emerald deposition. Considering the existence of emerald-bearing extension veins, a hydrostatic confining pressure ($P_{fluid} < P_{solid}$) could also have prevailed during the infilling of veins. Therefore, the estimated pressure range (1.06–1.12 kbars) represents a maximum correction range for the extrapolated trapping temperature.

Discussion of the trapping pressure and temperature estimations

An estimate of a 1-kbar trapping temperature was made by Kozlowski et al. (1988) on the basis of decrepitation temperatures and the comparison of quartz and beryl hardness, which agrees with our estimate (1.06 and 1.12 kbars).

The trapping temperature estimated by Roedder (1982, 1984) was 518°C, whereas Kozlowski et al. (1988) proposed a T_h = 470°C with a pressure correction of about 100°C for the Achiote deposit. These temperatures are in marked contrast with our estimates for Coscuez (this study) and La Vega-San Juan (Giuliani et al., 1993); the fluid inclusion behavior on heating also seems to be different. Let us detail this point. The phase transitions and fluid behavior near the vapor-saturated solubility surface of an inclusion containing a crystal of halite, a brine, and a gas phase will depend, for a given bulk composition, on the value of the bulk density and the liquid density of the fluid inclusion (Roedder and Bodnar, 1980; Sterner et al., 1988). Upon heating, an inclusion with a bulk density higher than the liquid density will first result in the disappearance of the vapor phase and then homogenization by salt dissolution, as illustrated by the microthermometric studies in the Coscuez (this work), La Vega-San Juan (Giuliani et al., 1993), and Muzo deposits (Ottaway and Wicks, 1986, 1991a, b). If the inclusion has a bulk density lower than the liq-

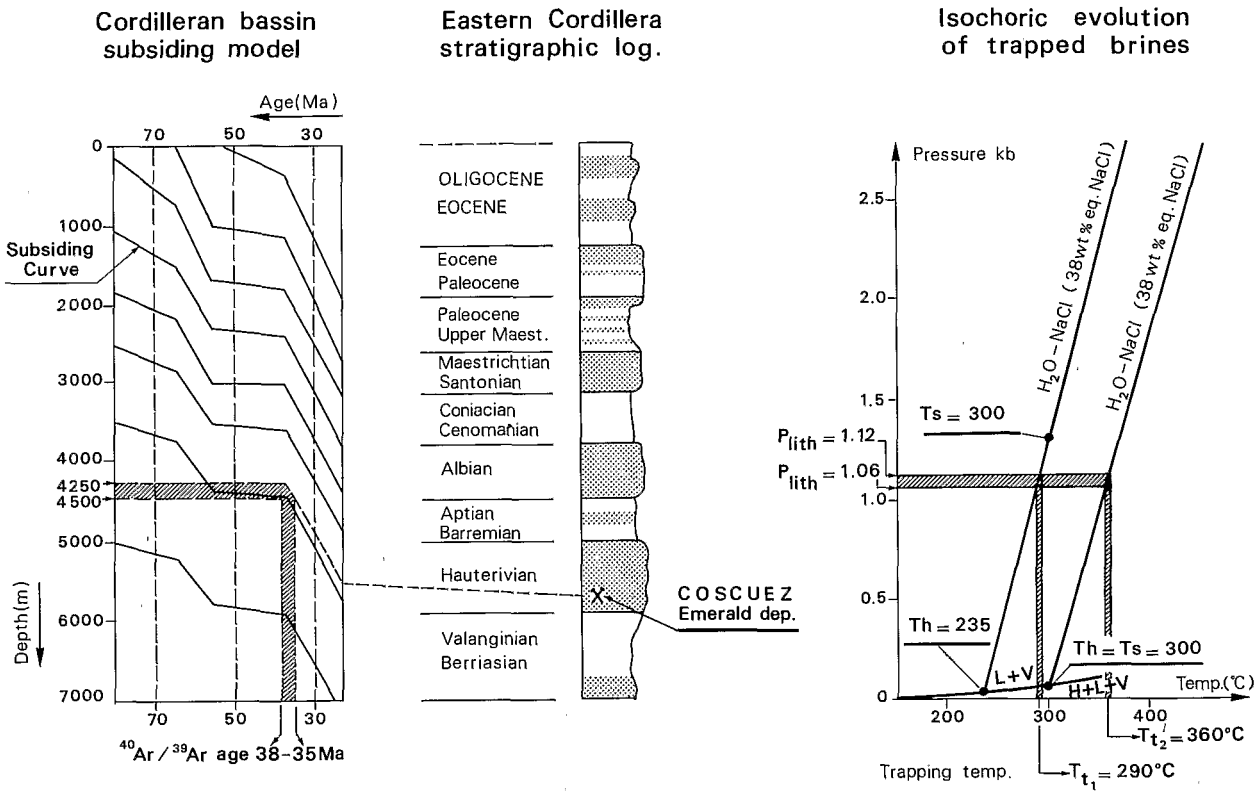

FIG. 11. Reconstruction of the thermobarometric constraints for emerald deposition in the Coscuez deposit, assuming lithostatic confining pressure conditions. The Cordilleran basin subsiding model is constructed after Hebrard (1985); the isochoric evolution of brines is derived from fluid inclusion data. Solid curve L + V-H + L + V is the three-phase, halite-saturated liquid-vapor curve in the H_2O-NaCl system. Th = temperature of homogenization of the vapor bubble; Ts = temperature of halite dissolution; salinities expressed as wt percent NaCl equiv.

uid's density, halite will first dissolve and further heating will result in total homogenization by vapor disappearance as described by Roedder (1982) and Kozlowski et al. (1988) for the Achiote deposit. This would imply that the fluid inclusion behavior in various emerald deposits of Colombia is different. Then, for halite-bearing fluid inclusions of a given composition, the pressure at homogenization will depend on the temperature and the order of disappearance of the different phases. Figure 11 shows that for inclusions having a bulk density equal to the liquid density (i.e., $T_h = T_s = 300°C$; isochore 2), the estimated trapping temperature $T_{trapping_2}$ is higher than $T_{trapping_1}$ estimated for $T_h < T_s$ (isochore 1). Furthermore, the contradictory results obtained for the fluid trapping temperature can be explained by poor data resulting from a possible heterogeneous trapping of the fluid, necking of fluid inclusions after a vapor phase has nucleated, and leakage during heating experiments. The first possibility of accidental entrapment of a halite crystal (identified by SEM; Giuliani et al., 1993) in a fluid inclusion would result in a higher homogenization temperature. Many primary fluid inclusions show variable liquid/vapor/halite ratios clearly resulting from necking. However, the consistency of our data for a small, closely spaced group of primary inclusions indicates that the fluid inclusions were trapped as a homogeneous fluid. As reported elsewhere by Robert and Kelly (1987), smaller inclusions within an individual healed microfracture or growth zone yield similar homogenization temperatures. We carefully selected the data in order to eliminate the leaked inclusions which gave the higher temperature ranges reported in the previous studies.

Finally, the calcite-dolomite-quartz-albite-muscovite-donbassite-kaolinite paragenesis that characterizes the mineralized veins appears to be in agreement with the proposed temperature range of precipitation of emerald (290°–360°C). Indeed, according to Merceron et al. (1988), the temperature of formation of donbassite can be estimated at $T < 350°C$. Moreover, the presence of the muscovite-kaolinite assemblage and the lack of pyrophyllite indicates a forma-

tion temperature below 350°C (Meyer and Hemley, 1967; Thomson, 1970; Tsuzuki and Mizutani, 1971).

Metallogenic Implications

The upper Eocene-lower Oligocene age of the Colombian emerald deposits confirms the hypothesis of Escovar (1979) and rules out the genetic link of the mineralizing fluid with the Lower Cretaceous basic magmatism (Ulloa, 1980). The composition-pressure-temperature characteristics of the hydrothermal brine-type fluids indicate moderate temperature for emerald mineralization (320° ± 40°C) as previously proposed by Beus and Mineev (1972). Considering the burial history of the Eastern Cordillera basin, thermal calculation by Hébrard et al. (1985) and Fabre (1987) indicate that temperatures of 210° and 240°C, respectively, have been reached by the end of the Cretaceous through simple subsidence. At the time of emerald mineralization, the hydrothermal fluid (320° ± 40°C) needed an additional 120° to 150°C thermal input with regard to the burial temperatures of the enclosing shales. Two possible heat sources might be suggested: synchronous magmatic intrusions as suggested by Escovar (1979) but yet not proved from field evidence, and heat conduction implemented during halokinetic ascent. Indeed, evaporitic plugs are known within Upper Cretaceous formations (Zipaquirá and Nemocon; MacLaughlin and Arce, 1971), a minimum Valanginian age being attributed to the salt deposition (Lopez et al., 1988). Therefore, salt diapirs might have been in contact or percolated by hydrothermal fluids. Gypsum pockets are found in the vicinity of the Chivor emerald district in the eastern mineralized belt. Following these observations, the source of the complex H_20-NaCl-KCl-$CaCl_2$ sulfate-rich brines (Giuliani et al., 1990b) are likely to be found through fluid interaction with the evaporitic beds. Sulfate reduction is evidenced at the Muzo deposit (Ottaway and Wicks, 1991b) and was probably responsible for the huge amount of pyrite precipitating in the emerald deposits. The sulfur isotope values of pyrite precipitating with emerald in four Colombian deposits ($15 < \delta^{34}S < 21.2‰$; Giuliani et al., 1993) are consistent with the Lower Cretaceous marine sulfate range ($15 < \delta^{34}S < 18‰$; Claypool et al., 1980). Oxygen and carbon isotope study of quartz and carbonates from emerald-bearing veins (Giuliani et al., 1992) showed large $\delta^{18}O$ values for the waters in equilibrium with the mineralization ($10 < \delta^{18}O < 18$) indicating a basinal formation waters origin. Derivation of CO_2 from a mixed oxydized organic matter and limestone source appears likely. Accompanying hydrothermal fluid circulation, a strong fluid-rock interaction process led to sodium and carbonate metasomatism development in the black shales (Beus, 1979). Geochemical profiles through the mineralized zones and mass balance calculation show that leaching of major (K, Al, Si, Ti, Mg, P) and trace elements (Ba, Be, Cr, Rb, Cs, U, V B, C, REE) from black shales is accompanied by their partial redistribution as infilling vein minerals (Giuliani et al., 1990d). Particularly indicative of this process is the leaching of REE from the black shales ($66 < \sum REE <$ 193 ppm, original content in the host rock) and subsequent redeposition as REE dolomite (previously known as codazzite) within the mineralized veins (Giuliani et al., 1990d). The origin of beryllium also may be local—i.e., shown by the large volume of metasomatized country rocks—as advocated by Baker (1975), Kozlowski et al. (1988), and E. Roedder (oral commun., 1992). Indeed, a simple balance calculation between a few parts per million of a Be-bearing country rock (0.6–3.0 ppm, following Beus and Mineev, 1972, or 1–5 ppm according to Escovar, 1979) and the amount of beryllium within a beryl crystal appears adequate to account for the 6-ppb emerald grade in the ore, as reported by Kozlowski et al. (1988) for the Quipama-Chivor mines. Our determination of the background Be content in the black shales away from the mineralized areas ranges between 3.4 and 4 ppm. These data confirm that the regional black shale reservoir was large enough to have been a potential beryllium source.

Tectonic Consequences

As suggested by Mégard (1987), the Eastern Cordillera constitutes an inverted sedimentary back-arc basin of Jurassic to Late Cretaceous age filled with thick accumulations of marine sediments; Eocene to late Oligocene synorogenic nonmarine molasse sequences buried the basin as a response to uplift of the Central Cordillera. Inversion of the Eastern Cordillera basin occurred during the Andean compressional episodes at late Miocene to Pliocene time. Two distinct upper Eocene to lower Oligocene ages have been determined for the emerald deposits of Coscuez (35–38 Ma) and Muzo-Quipama (31.5–32.6 Ma); if assigned to the tectonic evolution of the Eastern Cordillera, these ages are synchronous with a strong shortening episode starting during the Eocene and corresponding to an acceleration of the convergence rate between the Nazca and South American plates (Daly, 1989). At that time, sedimentation in the Eastern Cordillera basin was changing to nonmarine clastic deposition, whereas the underlying Mesozoic series were affected by alternating compressive and extensive transpressive episodes (Stephan et al., 1980; Calais et al., 1989) in response to crustal shortening. Emerald formation at 31 to 38 Ma appears to be a good example of this strong change in the tectonic regime of the Colombian Andes.

Following that period, major crustal deformation involved collisional regime between the Caribbean arc system and South America, leading to thrusting

and uplift of the Eastern Cordillera during late Miocene to Pliocene time, particularly through rejuvenation of the older limits of the Cretaceous basin (Fig. 1). These structures were characterized by low-angle thrusting, decollement levels, and associated opposite-verging folding and ramping on both fronts of the chain (Fig. 1; Colleta et al., 1990). They are free of any significant thermal anomaly (Hébrard, 1985) and clearly crosscut the vein systems associated with emerald mineralization. Considering the depth of formation of emerald (4,250–4,500 m), a minimum of 6,000 m of vertical transfer (excluding erosion) can be attributed to the late Miocene to Pliocene tectonic episodes which were responsible for the inversion of the Cretaceous back-arc basin and emerald outcropping.

Conclusions

This first determination of ages of the Colombian emerald deposits of Coscuez (35–38 Ma) and Muzo-Quipama (31.5–32.6 Ma) using induction and laser step-heating plus in situ laser spot fusion $^{40}Ar/^{39}Ar$ experiments on synchronous green muscovite allowed the estimation of PVT characteristics of the mineralizing complex brines (P = 1.2–1.06 kbars; T = 320° ± 20°C, and bulk salinity = 38 wt % NaCl equiv) as deduced from fluid inclusion microthermometric, and Raman microprobe data. Considered in the context of the paleogeodynamic evolution of the Colombian Andes, these results have important implications for the metallogenesis of the emerald deposits.

The location of the Colombian emerald deposits within two belts along the original limits of the Eastern Cordillera Cretaceous basin suggests that they might constitute deep-seated rejuvenated faults allowing hot fluid circulation up through the sedimentary pile and evaporitic beds. Hydrofracturing, strongly reducing environment, and metasomatic transfer through brines and black shale interaction then provoked emerald-calcite-pyrite-albite precipitation. The chemical composition of the fluid associated with emerald deposition belongs to the complex H_2O-NaCl-$CaCl_2$-KCl-CO_2-N_2 and sulfate-rich system. Similar fluids are associated with Cu-Pb-Zn deposits related to salt diapirs (Guilhaumou et al., 1981; Charef and Sheppard, 1987), metamorphosed evaporites (Mc Kibben et al., 1988), and the Tethysian margin during alpine tectonic evolution (Edon, 1993). The importance of complex brines and organic-rich sediments is also well documented for the genesis of Pb-Zn Mississippi Valley-type hydrothermal sedimentary deposits (Price et al., 1983; Sverjensky, 1986), although lower formation temperatures are generally recognized (200°–250°C).

Constrained by these new geologic and geochemical parameters, the genesis of the Colombian emerald deposits appears clearly independent of a magmatic cycle and must be related to the sedimentary features of basin margins constituted by thick black shale sequences and evaporitic beds. The temporal evolution of the basin through tectonic influence promotes hydrothermal basin-derived fluid circulation, highly reactive brine formation through partial dissolution of evaporitic beds and subsequent mobilization of metallic components (Be-Cr-V) from the enclosing shale; tectonic movements favored hydrothermal fluid circulation and epigenetic mineral precipitation within extension vein networks and hydraulic breccias.

According to our study, an epigenetic hydrothermal-sedimentary model is proposed for the Colombian emerald deposits, thus constituting an unique exemplar in the world. Considered within the scope of sedimentary basin dynamic, the Colombian emerald genesis must be related to thermal, hydraulic, and mechanical phenomena affecting the Eastern Cordillera basin; in that sense, it can be compared, although at higher temperature, to maturation, migration, and trapping of oil.

Acknowledgments

Laboratory and field studies were funded by grants from the ATP PIRSEM to A.C., from ORSTOM, Department TOA, UR 1H, to G.G., and from CNRS-CRPG to A.C. and G.G. Field studies were carried out with the logistical cooperation of ECOMINAS (1988), and then MINERALCO SA (1991) through the supervision of Vicente Giordanelli and J. Cuevas Bustos, respectively. A.C., G.G., and C.R. thank Felix Rueda (MINERALCO SA) and mining operators in Coscuez (ESMERACOL SA) and Quipama (COEXMINA) for their helpful assistance. D. Beaufort (XRD), M. Chaussidon (ion microprobe), M. Vernet (chemical analysis), J.M. Claude (microprobe), and J.L. Zimmermann (K-Ar) performed the respective analyses. S. Scaillet and Y. Ageon greatly contributed to the argon isotope analyses through discussion and advice regarding analytical procedures. J. Gerbaut typed the tables and Y. Lestreit carefully drafted the illustrations. E. Roedder, A. Koslowski, and J. Reynolds are thanked for their great assistance in a critical reading of a first draft of the manuscript. The three *Economic Geology* reviewers are greatly thanked for their encouraging suggestions.

April 20, 1992; August 28, 1993

REFERENCES

Baker, P.J., 1975, Projecto de esmeraldas, UNDP-Ingeominas final technical report: Instituto de Investigaciones en Geociencias, Minería y Chimíca [Bogotá], unpublished report, 71 p.

Beaufort, D., Dudoignon, P., Proust, D., Parneix, J.C., and Meunier, A., 1983, Microdrilling in thin section: A useful method for identification of clay minerals in situ: Clay Minerals, v. 18, p. 219–222.

Beus, A.A., 1979, Sodium: A geochemical indicator of emerald mineralization in the Cordillera Oriental, Colombia: Journal of Geochemical Exploration, v. 11, p. 195–208.

Beus, A.A. and Mineev, D.A., 1972, Some geological and geochemical features of the Muzo-Coscuez emerald zone, Cordillera oriental, Colombia: Instituto de Investigaciones en Geociencias, Minería y Chimíca [Bogotá], unpublished report, 50 p.

Bray, C.J., Spooner, E.T.C., Hall, C.M., York, D., Bills, T.M., and Krueger, H.W., 1987, Laser probe $^{40}Ar/^{39}Ar$ and conventional K/Ar dating of illites associated with the McClean unconformity-related uranium deposits, north Saskatchewan, Canada: Canadian Journal of Earth Sciences, v. 24, p. 10–23.

Brindley, G.W., 1980, Order-disorder in clay mineral structures, *in* Brindley G.W., and Brown G., eds., Crystal structures of clay minerals and their X-ray identification: Mineralogical Society [London] Monograph 5, p. 125–195.

Brown, P.E., and Lamb, W.M., 1989, PVT properties of fluids in the system $H_2O \pm CO_2 \pm NaCl$, new graphical presentations and implications for fluid inclusion studies: Geochimica et Cosmochimica Acta, v. 53, p. 1209–1221.

Calais, E., Stephan, J.F., Beck, C., Carfantan, J.C., Tardy, M., Thery, J.M., Olivet, J.L., Bouysse, P., Mercier de Lepinay, B., Tournon, J., Vila, J.M., Mauffret, A., Blanchet, R., Bourgois, J., and Dercourt, J., 1989, Evolution paléogéographique et structurale du domaine caraïbe du Lias à l'Actuel, 14 étapes pour 3 grandes périodes: Académie des Sciences [Paris] Comptes Rendus, v. 309, série II, p. 1437–1444.

Campbell, C.J., and Bürgl, M., 1965, Section through the Eastern Cordillera of Colombia, South America: Geological Society of America Bulletin, v. 76, p. 567–589.

Charef, A., and Sheppard, S.M.F., 1987, Pb-Zn mineralization associated with diapirism: Fluid inclusion and stable isotope (H,C,O) evidence for the origin and evolution of the fluids at Fedj-El-Aoum, Tunisia: Chemical Geology, v. 61, p. 113–134.

Claypool, G.E., Holer, W.T., Kaplan, I.R., Sakai, H., and Zak, I., 1980, The age curves of sulfur and oxygen isotopes in marine sulfate and their mutual interpretation: Chemical Geology, v. 28, p. 199–260.

Colleta, B., Hebrard, F., Letouzey, J., Werner, P., and Rudkiewicz J.L., 1990, Tectonic style and crustal structure of the Eastern Cordillera (Colombia) from a balanced cross-section, *in* Letouzey, J., ed., Petroleum and tectonics in mobile belts: Paris, Technips, p. 81–100.

Crawford, M.L.,1981, Phase equilibria in aqueous fluid inclusions: Mineralogical Association of Canada Short Course Handbook, v. 6, p. 75–100.

Daly, M.C., 1989, Correlations between Nazca/Farallon plate kinematics and forearc basin evolution in Ecuador: Tectonics, v. 8, p. 769–790.

Deer, W.A., Howie, R.A., and Zussman, J., 1962, Rock-forming minerals, Vol. 3, Sheet silicates: London, Longmans, Green and Co., 270 p.

Dubessy, J., Poty, B., and Ramboz, C., 1989, Advances in C-O-H-N-S fluid-geochemistry based on micro-Raman spectrometric analysis of fluid inclusions: European Journal of Mineralogy, v. 1, p. 517–534.

Edon, M., 1993, Contribution à la caractérisation P-T-t-X des fluides et des néoformations dans le Trias en place ou diapirique et dans sa couverture sédimentaire dans le bassin Sud-Est (France): Unpublished doctoral thesis, Orléans, France, Université d'Orléans, 242 p.

Escovar, R.R., 1979, Geologia y geoquimica de las minas de esmeraldas de Gachalà, Cundinamarca: Boletin Geologico [Bogotá], v. 22, p. 116–153.

Fabre, A., 1987, Tectonique et génération d'hydrocarbures: Un modèle de l'évolution de la Cordillère Orientale de Colombie et du bassin des Llanos pendant le Crétacé et le Tertiaire: Archives des Sciences [Genève], v. 40, p. 145–190.

Fabre, A., and Delaloye, M., 1983, Intrusiones bàsicas cretácicas en las sedimentitas de la parte central de la cordillera oriental: Geologia Norandina, v. 6, p. 19–28.

Féraud, G., Gastaud, J., Auzende, J.M., Olivet, J.L., and Cornen, G., 1982, $^{40}Ar/^{39}Ar$ ages for the alkaline volcanism and the basement of Gorringe Bank, North Atlantic Ocean: Earth and Planetary Science Letters, v. 57, p. 211–226.

Féraud, G., York, D., Mével, C., Cornen, G., Hall, C.M., and Auzende, J.M., 1986, Additional $^{40}Ar/^{39}Ar$ dating of the basement and the alkaline volcanism of Gorringe Bank (Atlantic Ocean): Earth and Planetary Science Letters, v. 79, p. 255–269.

Forero, H.O., 1987, Esmeraldas: Publicationes geologicas [Bogotá], v. 3, p. 557–605.

Giuliani, G., Silva, L.J.H.D., and Couto, P., 1990a, Origin of emerald deposits of Brazil: Mineralium Deposita, v. 25, p. 57–64.

Giuliani, G., Rodriguez, C.T., and Rueda, F., 1990b, Les gisements d'émeraude de la Cordillère orientale de la Colombie: Nouvelles données métallogéniques: Mineralium Deposita, v. 25, p. 105–111.

Giuliani, G., Cheilletz, A., and Rodriguez, C.T., 1990c, Emerald deposits from Colombia: Chemical composition of fluid inclusions and origin [abs.]: Quadrennial IAGOD Symposium, 8th, Ottawa, Canada, August 12–18, 1990, p. 48–49.

—— 1990d, New metallogenic data on the emerald deposits of Colombia [abs.]: Quadrennial IAGOD Symposium, 8th, Ottawa, Canada, August 12–18, 1990, p. 185–186.

Giuliani, G., Sheppard, S.M.F., Cheilletz, A., and Rodriguez, C.T,1992, Fluid inclusions and $^{18}O/^{16}O$, $^{13}C/^{12}C$ isotope geochemistry contribution to the genesis of emerald deposits from the Oriental Cordillera of Colombia: Académie des Sciences [Paris] Comptes Rendus, v. 314, série II, p. 269–274.

Giuliani, G., Cheilletz, A., Dubessy, J., and Rodriguez, C.T., 1993, Chemical composition of fluid inclusions in Colombian emerald deposits, *in* Maurice, Y.T., ed., Proceedings of the eighth quadrennial IAGOD symposium, Ottawa, Canada, August 12–18, 1990: Stuttgart, E. Schweizerbart'sche Verlagsbuchhandlung, p. 159–168.

Gubelin, E.J., 1957, A contribution to the genealogy of inclusions: Journal of Gemmology, v. 6, p. 1–47.

Guilhaumou, N., Dhamelincourt, P., Touray, J.C., and Touret, J., 1981, Etude des inclusions fluides du système N_2-CO_2 de dolomites et de quartz de Tunisie septentrionale. Données de la microcryoscopie et de l'analyse à la microsonde à effet Raman: Geochimica et Cosmochimica Acta, v. 45, p. 657–673.

Hall, C.M., Walter, R.C., Westgate, J.A., and York, D., 1984, Geochronology, stratigraphy and geochemistry of Cindery Tuff in Pliocene hominid-bearing sediments of the Middle Awash, Ethiopia: Nature, v. 308, p. 26–31.

Hall, D.L., Sterner, S.M. and Bodnar, R.J., 1988, Freezing point depression of NaCl-KCl-H_2O solutions: ECONOMIC GEOLOGY, v. 83, p. 197–202.

Hébrard, F., 1985, Les foot-hills de la Cordillère Orientale de la Colombie entre les rios Casanare et Cusiana. Evolution géodynamique depuis l'Eo-Crétacé: Unpublished doctoral thesis, Paris, France, Université Pierre et Marie Curie, 162 p.

Hébrard, F., Leikine, M., Bourgeois, J., Ricateau, R., and Charita, P., 1985, Métamorphisme et diagenèse des séries crétacées et tertiaires du flanc Est de la Cordillère Orientale de Colombie et de ses "Foot-Hills": Un exemple d'évolution thermique liée à l'ouverture d'un bassin subandin au Crétacé: Simposio bolivariano Exploracion Petrolera en las Cuencas Subandinas, 2nd, August 13–16, 1985, Bogotá, Proceedings, (not paginated).

Julivert, M., 1970, Cover and basement tectonics in the Cordillera Oriental of Colombia, and a comparison with other folded chains: Geological Society of America Bulletin, v. 81, p. 3623–3646.

Kazmi, A.H., and Snee, L.W., 1989, Emeralds of Pakistan. Geology, gemology and genesis, *in* Kazmi, A.H., and Snee, L.W., eds., Geological survey of Pakistan: New York, Van Nostrand Reinhold Co., 269 p.

Kozlowski, A., Metz, P., and Jaramillo, H.A.E., 1988, Emeralds from Somondoco, Colombia: Chemical composition, fluid inclusions and origin: Neues Jahrbuch für Mineralogie Abhandlungen, v. 159, p. 23–49.

Lo, C.H., and Onstott, T.C., 1989, ^{39}Ar recoil artefact in chloritized biotite: Geochimica et Cosmochimica Acta, v. 53, p. 2697–2711.

Lopez, C., Briceno, A., and Buitrago, J., 1988, Edad y origen de los diapiros de sal de la sabana de Bogota: Simposio Bolivariano Exploracion Petrolera en las Cuencas Subandinas, 3rd, August 1988, Bogotá, Proceedings, (not paginated).

MacLaughlin, D., and Arce, M., 1971, Recursos minerales de parte de los departamentos de Cundinamarca, Boyacà y Meta: Boletin Geologico [Bogotá], v. 19, no. 1, p. 1–102.

McKibben, M.A., Williams, A.E., and Okuko, S., 1988, Metamorphosed Plio-Pleistocene evaporites and the origins of hypersaline brines in the Salton Sea geothermal system, California: Fluid inclusions evidence: Geochimica et Cosmochimica Acta, v. 52, p. 1047–1056.

Mégard, F., 1987, Cordilleran Andes and marginal Andes: A review of Andean geology north of the Arica elbow (18 deg. S): American Geophysical Union Geodynamics Series, v. 18, p. 71–95.

Merceron, T., Inoue, A., Bouchet, A., and Meunier, A., 1988, Lithium-bearing donbassite and tosudite from Echassières, Massif Central, France: Clays and Clay Minerals, v. 36, p. 39–46.

Meyer, C., and Hemley, J.J., 1967, Wall rock alteration, *in* Barnes, H.L., ed., Geochemistry of hydrothermal ore deposits: New York, Holt, Rinehart, Winston, p. 166–235.

Odin, G.S., and Montanari, A., 1989, Age radiométrique et stratotype de la limite Eocène-Oligocène: Académie des Sciences [Paris] Comptes Rendus, v. 309, série II, p. 1939–1945.

Oppenheim, V., 1948, The Muzo emerald zone, Colombia S.A.: ECONOMIC GEOLOGY, v. 43, p. 31–38.

Ottaway, T.L., and Wicks, F.J., 1986, Characteristics and origin of the Muzo emerald deposit, Colombia [abs.]: International Mineralogical Association Meeting Abstracts with Programs, Los Angeles, California, p. 113.

—— 1991a, The $20,000 question: What's missing in Colombian emeralds? [abs.]: International Gemological Symposium, June 20–24, 1991, Los Angeles, California, p. 156.

—— 1991b, Sulfate reduction at the Muzo emerald deposit, Colombia [abs.]: Geological Association of Canada Program with Abstracts, v. 16, p. A 93.

Potter, R.W., and Brown, D.L., 1975, The volumetric properties of aqueous sodium chloride solutions from O° to 500°C and pressures up to 2000 bars based on a regression of available data in the literature: U.S. Geological Survey Open-File Report 75–636, 31 p.

Poty, B., Leroy, J., and Jachimowicz, L., 1976, Un nouvel appareil pour la mesure des températures sous le microscope: l'Installation de microthermométrie Chaixmeca: Société Française de Minéralogie et Cristallographie Bulletin, v. 99, p. 182–186.

Price, P.E., Kyle, J.R., and Wessel, G.R., 1983, Salt dome related zinc-lead deposits, *in* Kisvarsanyi G., Grant S.K., Pratt, W.P., and Koenig, J.W., eds., International conference on Mississipi Valley type lead-zinc deposits. Proceedings volume: Rolla, University of Missouri-Rolla, p. 558–570.

Rassineux, F., Beaufort, D., Merceron, T., Bouchet, A., and Meunier, A., 1987, Diffraction sur lame mince pétrographique avec un détecteur à localisation linéaire: Analusis, v. 15, no 7, p. 333–336.

Robert, F., and Kelly, W.C., 1987, Ore-forming fluids in Archean gold-bearing quartz veins at the Sigma mine, Abitibi greenstone belt, Quebec, Canada: ECONOMIC GEOLOGY, v. 82, p. 1464–1482.

Roedder, E., 1963, Studies of fluid inclusions II: Freezing data and their interpretation: ECONOMIC GEOLOGY, v. 58, p. 163–211.

—— 1982, Fluid inclusions in gemstones: Valuable defects: International Gemmological Symposium, Santa Monica, California, Proceedings, p. 479–502.

—— 1984, Fluid inclusions: Reviews in Mineralogy, v. 12, 644 p.

Roedder, E., and Bodnar, R.J., 1980, Geologic pressure determinations from fluid inclusions studies: Annual Review of Earth and Planetary Sciences, v. 8, p. 263–301.

Rosasco, G.J., and Roedder, E., 1979, Application of a new Raman microprobe spectrometer to nondestructive analysis of sulfate and other ions in individual phases in fluid inclusions in minerals: Geochimica et Cosmochimica Acta, v. 43, p. 1907–1915.

Rudowski, L., Giuliani, G., and Sabaté, P., 1987, Les phlogopitites à émeraude au voisinage des granites de Campo Formoso et Canaiba (Bahia, Brésil): un Exemple de minéralisation protérozoique à Be, Mo et W dans les ultrabasites métasomatisées: Académie des Sciences [Paris] Comptes Rendus, v. 301, série II, p. 1129–1134.

Ruffet, G., Féraud, G., and Amouric, M., 1991, Comparison of ^{40}Ar/^{39}Ar conventional and laser dating of biotites from the North Trégor batholith: Geochimica et Cosmochimica Acta, v. 55, p. 1675–1688.

Scaillet, S., Féraud, G., Lagabrielle, Y., Ballèvre, M., and Ruffet, G., 1990, ^{40}Ar/^{39}Ar laser-probe dating by step heating and spot fusion of phengites from the Dora Maira nappe of the western Alps, Italy: Geology, v. 18, p. 741–744.

Stephan, J.F., Beck, C., Bellizzia, A., and Blanchet, R., 1980, La chaîne Caraïbe du Pacifique à l'Atlantique: Bureau Recherches Géologiques et Minières Memoire 115, p. 38–59.

Steiger, R.H., and Jäger, E., 1977, Subcommission on geochronology: Convention on the use of decay constants in geo- and cosmo-chronology: Earth and Planetary Science Letters, v. 36, p. 359–362.

Sterner, S.M., Hall, D.L., and Bodnar, J., 1988, Synthetic fluid inclusions, V: Solubility reactions in the system NaCl-KCl-$H_2$0 under vapor saturated conditions: Geochimica et Cosmochimica Acta, v. 52, p. 989–1005.

Sverjensky, D.A., 1986, Genesis of Mississipi Valley-type lead-zinc deposits: Annual Review of Earth and Planetary Sciences, v. 14, p. 177–199.

Thomson, A.B., 1970, A note on the kaolinite-pyrophyllite equilibrium: American Journal of Earth Sciences, v. 268, p. 454–458.

Touray, J.C. and Poirot, J.P., 1968, Observations sur les inclusions fluides primaires de l'émeraude et leurs relations avec les inclusions solides: Académie des Sciences [Paris] Comptes Rendus, v. 266, série D, p. 305–308.

Tsuzuki, Y., and Mizutani, S., 1971, A study of rock alteration process based on kinetics of hydrothermal experiment: Contributions to Mineralogy and Petrology, v. 30, p. 15–33.

Turner, G., and Cadogan, P.H., 1974, Possible effects of ^{39}Ar recoil in ^{40}Ar/^{39}Ar dating: Lunar Science Conference, 5th, Houston, Texas, March 18–22, 1974, Proceedings, p. 1601–1615.

Ulloa, C., 1980, Ambiente geologico de los yacimientos esmeraldiferos en Colombia: Sociedad Geologica de Lima Boletin, v. 65, p. 157–170.

Ulloa, C., and Rodriguez, E. 1979, Geological del cuadrangulo K-12, Guatèque: Boletin Geologico [Bogotá], v. 22, p. 1–55.

Vanko, D.A., Bodnar, R.J., and Sterner, S.M., 1988, Synthetic fluid inclusions, VIII: Vapor-saturated halite solubility in part of the system NaCl-$CaCl_2$-H_2O with application to fluid inclusions from oceanic hydrothermal systems: Geochimica et Cosmochimica Acta, v. 52, p. 2451–2456.

Zimmermann, J.L., Vernet, M., Guyetand, G., and Dautel, D., 1985, Données sur potassium et argon (de 1976 à 1984) dans quelques échantillons géochimiques de référence: Geostandards Newsletters, v. 9, p. 205–208.